X-ray switch for rare earth element adsorption to a liquid interface

Pan Sun[1,2]*, Erik A. Binter[1], Bikash Sapkota[1], M. Alex Brown[3], Artem V. Gelis[4], Mrinal K. Bera[2], Binhua Lin[2], Wei Bu[2]*, Mark L. Schlossman[1]*

[1]Department of Physics, University of Illinois at Chicago, Chicago, IL 60607, USA.

[2]NSF's ChemMatCARS, Pritzker School of Molecular Engineering, University of Chicago, Chicago, IL 60637, USA.

[3]Chemical and Fuel Cycle Technologies Division, Argonne National Laboratory, Lemont, IL, 60439, USA.

[4]Radiochemistry Program, Department of Chemistry and Biochemistry, University of Nevada, Las Vegas, NV, 89141, USA.

*Corresponding authors: Pan Sun, Wei Bu, Mark L. Schlossman
*E-mail: sunp@ornl.gov, weibu@uchicago.edu, schloss@uic.edu.

ORCID:
Pan Sun: 0000-0002-6128-8656
Erik A. Binter: 0000-0002-0520-3056
Bikash Sapkota: 0000-0001-8204-9673
M. Alex Brown: 0000-0002-6223-561X
Artem V. Gelis: 0000-0002-5487-1472
Mrinal Bera: 0000-0003-0698-5253
Binhua Lin: 0000-0001-5932-4905
Wei Bu: 0000-0002-9996-3733
Mark L. Schlossman: 0000-0003-3238-1250

Competing Interest Statement: The authors declare no competing interest.
Keywords: reversible adsorption, lanthanides, liquid interfaces, X-ray exposure, chemical separation

Abstract

Reversible cycling of rare earth lanthanide elements between an electrolyte solution and its free surface is achieved by X-ray exposure which alters the competitive equilibrium between lanthanide ions bound to a chelating ligand, DTPA, in the bulk liquid and to insoluble monolayers of extractant DHDP at its surface. Evidence for the exposure-induced temporal variations in the lanthanide surface density is provided by X-ray fluorescence near total reflection measurements. Varying the X-ray penetration depth between 10 nm and 2.8 μm separates surface and bulk processes which identifies the role of aqueous radiolysis in the adsorption cycle. Comparison of different chelates identifies amine binding sites as a contributor to the cycling mechanism. The primary molecules, DTPA and DHDP, are like those used in the separation of lanthanides from ores and in the reprocessing of nuclear fuel. Controllably dosing a liquid interface with lanthanides could trigger a range of interfacial processes, including enhanced metal ion extraction, catalysis, and interfacial phase transitions.

Introduction

Ions at liquid interfaces play a central role in many processes, including materials development where they influence molecular and particle assembly,[1-5] and chemical separations where they determine the efficiency and selectivity of critical element recovery.[6-11] Many of these interfacial processes rely upon neighboring bulk phases as a reservoir of ions. Such processes can be influenced by controlling the properties of the reservoir, such as the concentration of free ions available to be transported to the interface. Control over this transport, from bulk to interface and back, can lead to the triggering of interfacial processes as demonstrated by electrochemical methods for the liquid-liquid interface between two immiscible electrolyte solutions.[12,13] Here, we demonstrate that exposure to X-rays provides a method to move rare earth lanthanide ions between bulk liquid and its liquid-vapor interface. This method utilizes complexants and extractants like those used in solvent extraction processes to separate and purify lanthanides and actinides.

Rare earth elements are used in many advanced technologies, including permanent magnets,[14] supercapacitors,[15] superconductivity,[16] and sustainable energy systems.[17] Solvent extraction processes to separate and purify rare earth ions from multi-component aqueous mixtures involve placing the aqueous phase in contact with an organic phase containing amphiphilic extractant molecules that interact with the targeted ions and transport them into the organic phase for further processing.[18,19] Extractants are believed to complex with ions at the interface, and recent studies have suggested that complexation of ions with extractants in the bulk aqueous phase is not advantageous to the intended extraction.[20] Nevertheless, other molecules, denoted aqueous complexants, are utilized to complex with specific ions in the bulk aqueous phase, preventing them from interacting with extractants and being extracted into the organic phase. This has been used to advance the separation of actinides and lanthanides, where complexants such as DTPA hold back actinides in the aqueous phase while lanthanides are extracted into the organic phase.[21,22]

The competing effects of extractants and complexants contribute to the equilibrium distribution of ions in bulk and interfacial liquids. The concentration and type of extractants and complexants, as well as the pH, temperature, the choice of solvents, and the target ions are the primary variables used to control extraction.[23] Kinetics (diffusive or molecular) can also enhance the fractionation of ions.[24] Here, we introduce another variable and demonstrate that the equilibrium ion distribution can be altered by exposing the bulk liquid to X-rays, thereby producing a controllable and reversible transport of ions between bulk liquid and a liquid-vapor interface. It is known that aqueous radiolysis produces H and OH radicals, as well as hydrated electrons that react with a wide

range of solutes, which have been implicated in the reprocessing of nuclear fuel.[25,26] These products of aqueous radiolysis are likely responsible for the effects reported here.

The temporal evolution towards a new equilibrium state is probed by X-ray fluorescence near total reflection (XFNTR), a technique that measures the element-specific surface density of ions at the interface.[27] XFNTR measurements of 5 seconds duration allow us to vary the X-ray exposure while measuring the surface density of ions. Continuous XFNTR measurements maximize the total exposure, while infrequent measurements without X-ray exposure between them are used to minimize the total exposure of the sample. X-ray exposure effects are probed by experiments that vary the X-ray penetration depth and the aqueous pH, as well as utilize different complexants and rare earth ions. A simple model of the kinetics summarizes the approach to equilibrium of the transport of ions from bulk liquid to interface and back. These experiments demonstrate a method to reversibly control the availability of rare earth ions at liquid interfaces.

Results and Discussion

Reversible cycling of Nd adsorption Controlled and reversible adsorption of rare earth neodymium ions to the water-vapor interface was implemented by altering the competitive equilibrium between Nd^{3+} bound to a chelating ligand DTPA (Fig. 1A) dissolved in water and to an insoluble monolayer of DHDP (Fig. 1A) spread on the water surface. Exposure of the water surface and nearby bulk solution to 10 keV X-rays alters the equilibrium between these two bound complexes, leading to the reversible transport of ions between surface and bulk liquid as illustrated schematically in Figs. 1B and 1C. X-ray exposure releases Nd^{3+} ions bound to DTPA, allowing them to bind to the DHDP monolayer (Fig. 1B). Removing the continuous exposure of X-rays allows the DTPA to dominate the binding equilibrium once again and Nd^{3+} ions leave the surface to bind to DTPA in the bulk aqueous phase (Fig. 1C).

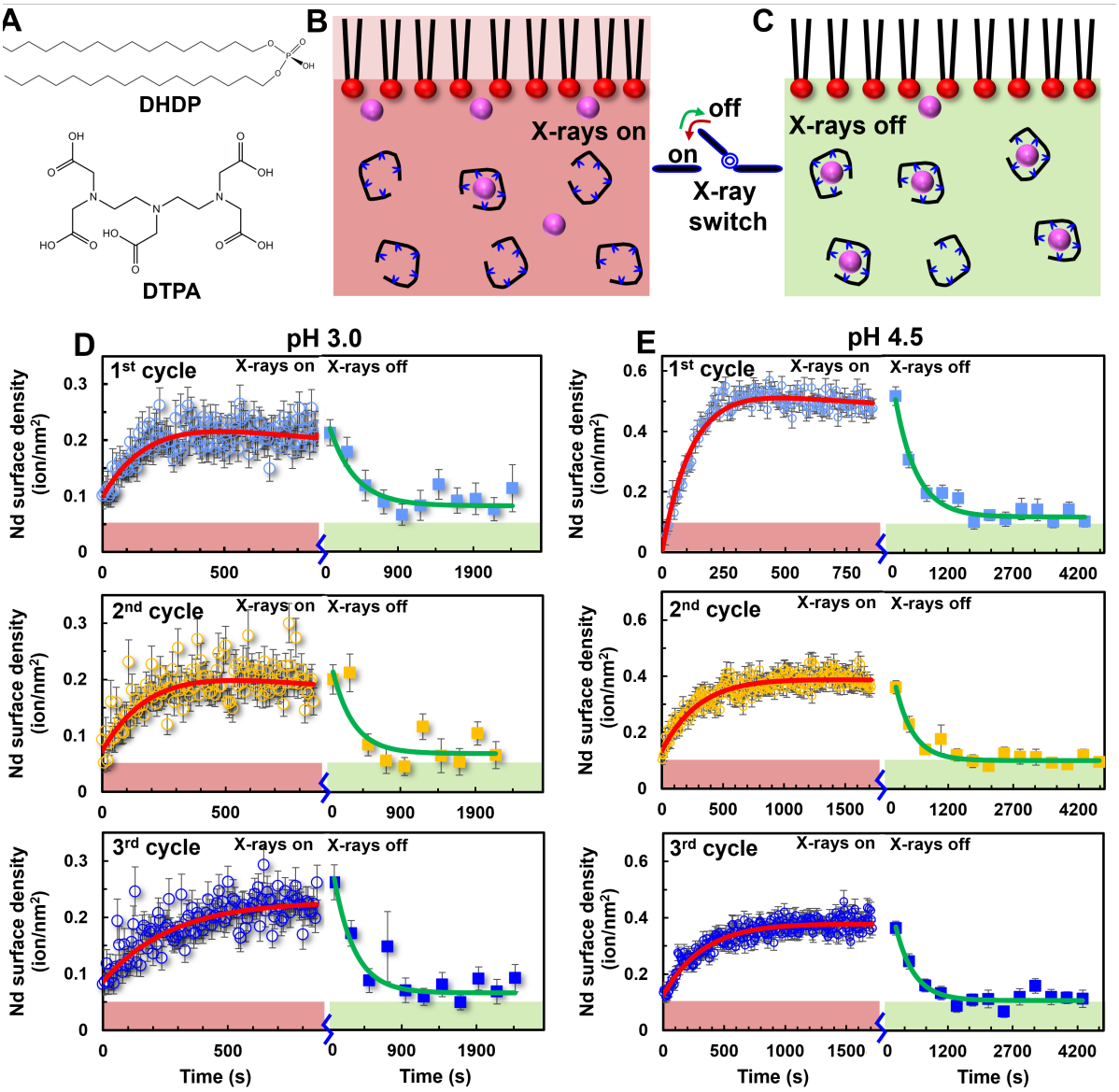

Figure 1. The effect of cycling X-ray exposure on the surface adsorption of Nd^{3+}. A monolayer of DHDP is held at a surface pressure of 10 mN/m on the surface of water containing 30 μM DTPA, which is a chelating agent, and 10 μM $NdCl_3$. (A) DHDP (dihexadecyl phosphoric acid) and DTPA (diethylenetriamine pentaacetic acid). (B) Illustration of the X-rays-on steady state with a high surface density of ions. Ions are colored magenta, DHDP monolayer at the surface with red phosphoric acid headgroups and black alkyl chains, and DTPA in the bulk (black cages). Red background indicates that X-rays expose the surface and bulk. (C) Illustration of the X-rays-off steady state with a low surface density of ions and most ions bound to DTPA in the bulk aqueous solution shown in green. (D, E) Temporal evolution of the Nd surface density measured for three cycles at aqueous pH of (D) 3.0 and (E) 4.5. Each cycle consists of an X-ray exposure ("X-rays on") and subsequent recovery ("X-rays off"). X-rays-on refers to continuous exposure of the sample to X-rays with ongoing XFNTR measurements of 5 seconds duration. X-rays-off refers to a 5-second XFNTR

measurement every 5 minutes without X-ray exposure between measurements. Times marked "0" indicate when the X-rays-on or X-rays-off step started. The color strip at the bottom of each panel also identifies the X-ray exposure (red for on, green for off). X-ray exposures and measurements were made at Q_z = 0.025 Å^{-1}, which exposes both the surface and the bulk aqueous phase within a few micrometers of the surface. Lines are fits described later in the text.

Evidence for the controlled cycling of Nd^{3+} ions between the bulk and surface of the aqueous solution is shown in Fig. 1. Figures 1D and 1E show the temporal evolution of the surface density of Nd during three consecutive cycles of X-ray exposure. Each cycle consists of two steps: X-rays-on and X-rays-off. X-rays-on refers to continuous exposure of the sample to X-rays. During this exposure the element-specific surface density was measured by synchrotron X-ray fluorescence near total reflection (XFNTR, see Section S1 and Fig. S2 in the SI).[27] The X-ray fluorescence was generated by X-rays incident on the surface at an angle that is slightly above the angle for total reflection. These X-rays illuminate the surface region and transmit into the bulk aqueous phase with a penetration depth (normal to the surface) of 2.8 μm. XFNTR measurements last 5 seconds each and occur continuously during the X-rays-on exposure. X-rays-off refers to a greatly reduced exposure of the sample for which a 5-second XFNTR measurement occurs once every 5 minutes but without X-ray exposure between measurements. These experimental results were obtained from samples of a composition and pH for which DTPA is expected to chelate nearly 100% of the Nd^{3+} ions in solution in the absence of other molecules, such as the DHDP monolayer, or effects such as X-ray exposure (Fig. S1B). Figures 1D and 1E show that the surface density of Nd increases during the X-rays-on step and decreases during the X-rays-off step of each cycle.

Effect of X-ray exposure on DHDP and DTPA The measurements in Fig. 1D/E can be explained as the result of two aspects of X-ray exposure: unbinding of ions from the DHDP monolayer and unbinding of ions from DTPA. XFNTR measurements of the temporal evolution of the Nd surface density from samples without DTPA in the aqueous phase are shown in Figure 2. These measurements demonstrate that the surface density of Nd bound to the DHDP monolayer decreases with time when the sample is continuously exposed to X-rays. It is important to note that other authors have used XFNTR to measure stable surface densities of lanthanide and other ions bound to DHDP monolayers on the surface of water and we also present evidence of stable measurements in the SI (Fig. S3).[20,27] Stable measurements can be obtained by introducing absorber foils into the X-ray beam to reduce the X-ray flux below a critical value. The measurements in this paper used X-ray beam fluxes of 3 x 10^{10} photons/s which were roughly four times this critical value to achieve the measured effects (Section S2).

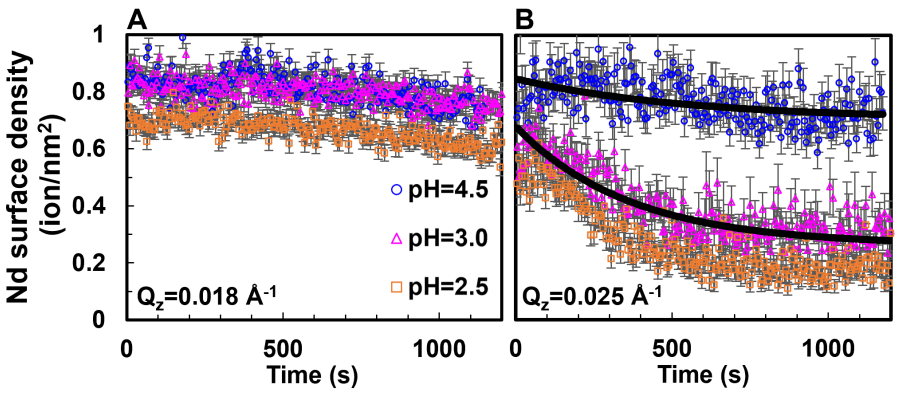

142

143 **Figure 2.** The effect of X-ray exposure on the desorption of Nd from a surface monolayer of DHDP in
144 the absence of DTPA. The monolayer was held at a surface pressure of 10 mN/m on the surface of
145 water containing 10 μM $NdCl_3$. XFNTR measurements of Nd surface density under continuous X-ray
146 exposure with (A) total reflection of X-rays at Q_z = 0.018 Å^{-1}, which exposes the surface region with a
147 penetration depth of 10 nm, and (B) X-ray reflection at Q_z = 0.025 Å^{-1}, which exposes the surface and
148 the bulk aqueous phase with a penetration depth of 2.8 μm. Values of pH are 4.5 (blue), 3.0 (magenta),
149 2.5 (orange). Two lines in (B) are fits described in the text.

150 The measurements in Fig. 2B were taken under similar conditions as those in Fig. 1, however,
151 the measurements in Fig. 2A were taken with X-rays reflected at a smaller angle of incidence, one
152 which is below the angle of total reflection. In this case, X-rays are totally reflected from the surface
153 at a wave vector transfer of Q_z = 0.018 Å^{-1}. Total reflection creates an evanescent wave of X-rays
154 whose penetration depth into the water is 10 nm, which is 280 times smaller than the penetration
155 depth when Q_z = 0.025 Å^{-1} (above the angle of total reflection) used for the measurements in Figs. 1
156 and 2B. Greater penetration of X-rays into the water exposes a greater volume of water to X-rays and
157 produces a larger decay of Nd surface density for pH $\leq$ 3.0, as illustrated by comparing Fig. 2B to Fig.
158 2A. This suggests that the radiolysis of water by X-rays produces species that interact with DHDP to
159 release Nd ions. The larger effects observed at lower pH in Fig. 2B are consistent with previous
160 reports of higher yields of radiolytic species in acidic media than in alkaline media.[28]

161 The XFNTR measurements shown in Fig. 2A and Fig. 2B were measured from the same sample
162 for a given value of pH. Measurements in Fig. 2A were taken first from one spot of the sample surface,
163 then the beam was moved to another spot for the measurements in Fig. 2B, with a time delay of about
164 2 minutes. Control experiments showed that the second spot was far enough from the first to be
165 unaffected by direct X-ray exposure of the first spot. The near equivalence of the final values of
166 surface density in Fig. 2A to the initial values in Fig. 2B shows that the temporal evolution in Fig. 2A
167 was due to X-ray exposure that affected the entire sample, not just the part of the sample within the

X-ray footprint. Ozone produced by X-rays in the vapor above the sample surface might be responsible for the changes observed in Fig. 2A, despite attempts to purge oxygen from the vapor by a helium flow. These effects were not observed at lower X-ray exposure (Fig. S3).

Figure 1 shows that the initial measurement in each cycle starts with a low surface density of Nd. For example, the first data point measured for pH 4.5 samples represents a surface density of 0.02 ions nm^{-2}. It will be shown later that the surface density of Nd remains at this low value for the duration of a long exposure when X-rays illuminate only the surface by reflecting at Q_z = 0.018 $Å^{-1}$, which is below the angle of total reflection. This suggests that either direct X-ray exposure of DTPA in the bulk water is required to release Nd ions from DTPA, or that radiolysis products from the bulk water are required to release Nd ions from DTPA. Released Nd ions are then free to diffuse to the surface and adsorb to DHDP.

Kinetics model of reversible adsorption cycling The effects of X-ray exposure are modeled to fit the Nd surface density data in Fig. 1D/E. The total Nd surface density under X-rays-on conditions, $n_{Nd}^{tot,on}$, was fit to the Nd surface density that desorbs from the surface, $n_{Nd}^{des,on}$, subtracted from the Nd surface density that adsorbs to the surface, $n_{Nd}^{ad,on}$,

$$n_{Nd}^{tot,on} = n_{Nd}^{ad,on} - n_{Nd}^{des,on} + b, \quad (1)$$

where the constant b represents the initial value of the ion surface density for the X-rays-on part of a cycle.

The adsorption process likely consists of several steps: release of Nd ions from DTPA dissolved in the aqueous phase, diffusion of Nd ions to the surface, and adsorption to the DHDP monolayer at the surface. The temporal variation of the surface density $n_{Nd}^{ad,on}$ is approximated by an exponential function,

$$n_{Nd}^{ad,on} = a(1 - e^{-k_1 t}), \quad (2)$$

where the constant a represents the increase in ion surface density due to X-ray exposure that would occur from t = 0 to ∞, and k_1 is an inverse time constant of the process.

The desorption process includes the unbinding of Nd ions from the DHDP monolayer due to X-ray exposure, as well as the diffusion of the ion out of the surface region. This process is modeled for pH 3.0 and pH 4.5 by fitting the data in Fig. 2B, which was measured in the absence of DTPA, to

196 an exponential decay, $ce^{-k_2 t} + d$. The amplitude c and constant k_2 were determined separately for
197 the pH 3.0 and pH 4.5 data in Fig. 2B, then used to parameterize the surface density $n_{Nd}^{des,on}$,

198 $$n_{Nd}^{des,on} = c(1 - e^{-k_2 t}), \quad (3)$$

199 where the constant c represents the decrease in ion surface density due to X-ray exposure that would
200 occur from t = 0 to ∞, and k_2 is an inverse time constant of the process.

201 Substituting Eqs. (2) and (3) into Eq. (1) yields an expression used to fit the data in Fig. 1
202 measured under X-rays-on conditions,

203 $$n_{Nd}^{tot,on} = a(1 - e^{-k_1 t}) + b - c(1 - e^{-k_2 t}). \quad (4)$$

204 Values of c and k_2 were taken from the fits to the data shown in Fig. 2B, then used to fit a, b, and
205 k_1 to the X-rays-on data in Fig. 1, separately for each pH and cycle. Note that the sum $a + b - c$ is
206 the steady state value if $t \to \infty$ under X-rays-on conditions.

207 The X-rays-off process shown in Fig. 1 represents the release of Nd ions from the DHDP
208 monolayer to bind, presumably, to the DTPA in the bulk water. The total Nd surface density under X-
209 rays-off conditions $n_{Nd}^{tot,off}$ was fit to the data in Fig. 1 with an exponential,

210 $$n_{Nd}^{tot,off} = fe^{-k_3 t} + g, \quad (5)$$

211 where f, g, and k_3 are constants determined by fitting and g is the steady state value if $t \to \infty$ under
212 X-rays-off conditions. The fitted parameters to the X-rays-on and X-rays-off data in Fig. 1 are
213 provided in Table 1.

214 The inverse rate constants in Table 1 have values on the order of hundreds of seconds, which
215 likely reveals the diffusive nature and complexity of each process in the model. For example, k_1
216 characterizes a process which could involve X-rays producing radiolysis products that diffuse to
217 DTPA, releasing Nd ions which then diffuse to the surface and bind to DHDP. Alternatively, k_1 could
218 represent the effect of direct release of Nd ions by X-ray exposure but would still involve diffusion of
219 Nd ions from DTPA in the bulk water to DHDP at the surface. Similarly, the constant k_2 for pH 3.0
220 samples involves the production of radiolysis products in the bulk water which diffuse to DHDP at
221 the surface to release Nd ions, though the constant k_2 for pH 4.5 data appears to represent an X-ray
222 exposure process independent of radiolysis effects. Finally, the constant k_3, which characterizes the
223 X-rays-off part of the cycle represents the equilibration between a strongly binding DTPA in bulk
224 water and a weaker binding DHDP at the surface when the initial condition contains an excess of ions

at the surface. This process has a long time constant and may involve diffusion of DTPA to the surface region.

TABLE 1 Parameters from equations (3) and (4) used to fit the data in Fig. 1. Parameters k_2 and c are taken from fits to the data in Fig. 2B.

	pH 3.0				pH 4.5			
X-rays on	k_1 (10^{-3} s^{-1})	k_1^{-1} (s)	k_2 (10^{-3} s^{-1})*	a+b-c (ions/nm^2)	k_1 (10^{-3} s^{-1})	k_1^{-1} (s)	k_2 (10^{-3} s^{-1})*	a+b-c (ions/nm^2)
1st cycle	$3.8^{0.4}_{0.5}$	260^{30}_{30}	$2.8^{0.6}_{0.6}$	$0.18^{0.03}_{0.05}$	$7.9^{0.6}_{0.5}$	126^{9}_{8}	$1.8^{1.0}_{0.6}$	$0.47^{0.04}_{0.04}$
2nd	$3.7^{0.6}_{0.5}$	270^{40}_{30}	$2.8^{0.6}_{0.6}$	$0.17^{0.03}_{0.06}$	$2.8^{0.4}_{0.3}$	353^{49}_{41}	$1.8^{1.0}_{0.6}$	$0.38^{0.05}_{0.05}$
3rd	$3.0^{0.4}_{0.3}$	330^{50}_{40}	$2.8^{0.6}_{0.6}$	$0.23^{0.03}_{0.05}$	$2.6^{0.3}_{0.3}$	379^{48}_{41}	$1.8^{1.0}_{0.6}$	$0.38^{0.05}_{0.05}$
X-rays off	k_3 (10^{-3} s^{-1})	k_3^{-1} (s)	f (ions/nm^2)	g (ions/nm^2)	k_3 (10^{-3} s^{-1})	k_3^{-1} (s)	f (ions/nm^2)	g (ions/nm^2)
1st cycle	$2.9^{1.1}_{0.8}$	340^{130}_{90}	$0.14^{0.02}_{0.02}$	$0.08^{0.01}_{0.01}$	$2.0^{0.5}_{0.4}$	490^{110}_{90}	$0.39^{0.04}_{0.04}$	$0.12^{0.01}_{0.01}$
2nd	$3.6^{2.4}_{1.5}$	280^{190}_{110}	$0.15^{0.04}_{0.04}$	$0.07^{0.01}_{0.02}$	$2.5^{0.5}_{0.5}$	400^{90}_{70}	$0.26^{0.02}_{0.03}$	$0.10^{0.01}_{0.01}$
3rd	$3.6^{1.2}_{0.8}$	280^{90}_{60}	$0.20^{0.03}_{0.03}$	$0.07^{0.01}_{0.01}$	$2.4^{0.6}_{0.5}$	420^{110}_{90}	$0.26^{0.03}_{0.03}$	$0.11^{0.01}_{0.01}$

*For X-rays-on: $k_2^{-1}= 540^{300}_{160}$ for pH 3.0 and $k_2^{-1}=360^{120}_{80}$ (s) at pH 4.5. Superscripts represent a positive error bar and subscripts represent a negative error bar.

The one exception is the faster adsorption (k_1) that occurs during the first cycle for pH 4.5 samples, which was also observed when replacing Nd with Gd at this pH (Fig. S4). Faster adsorption is accompanied by an initial surface ion density that is small (0.02 ions nm^{-2}) compared with the value of 0.1 ions nm^{-2} observed at the beginning of subsequent cycles for pH 4.5 samples. We suggest that this effect could be the result of a non-equilibrium initial state at pH 4.5, possibly due to a large free energy barrier to unbind ions from DTPA at the higher pH. In this scenario, X-rays facilitate the release of ions over the large free energy barrier during the initial cycle and subsequent cycles are between equilibrium states. Such effects were not observed for pH 3.0.

The steady state values for the X-rays-on part of the cycle, given by $a + b - c$, and the steady state values for the X-rays-off part of the cycle, given by g, are larger for pH 4.5 samples than for those at pH 3.0. This represents the expected enhancement of bound Nd^{3+} over H^+ to DHDP at higher pH. This is consistent with the measured effective surface pK (= 1.9) of trivalent lanthanum binding to a monolayer of DHDP and known trends in liquid-liquid extraction of lanthanides with a similar extractant, bis(2-ethylhexyl) phosphoric acid (HDEHP).[29,30] The extraction constant of Nd^{3+} with HDEHP is approximately 15 and the extraction mechanism operates with a third-power H^+

dependence in which the equilibrium is shifted to the extracted complex at higher pH. The DTPA and the extractant compete generally between pH 2 and 4 but the distribution of Nd begins to increase past pH 4.5, indicating greater binding to the extractant at higher pH.[30]

Irreversibility at low pH X-ray exposure-induced adsorption cycles were not observed at lower pH. As an example, Fig. 3 shows data measured from pH 2 aqueous samples whose composition is the same as those in Figs. 1 and 2. The Nd surface density for X-rays-on measurements at Q_z = 0.025 Å^{-1} is the same in the absence or presence of DTPA (Fig. 3A). Although it might be expected that the radiolysis effects that released ions from DTPA at higher pH will also do so at lower pH because of the expected increase in radiolysis products at lower pH,[28] it appears that X-ray induced release of Nd ions from DTPA does not affect Nd binding to the DHDP monolayer. At this pH, DTPA is expected to chelate a reduced amount, roughly 40%, of the Nd^{3+} ions in solution in the absence of other molecules or effects (Fig. S1B). These results suggest that there are enough free Nd^{3+} to satisfy the adsorption needs of the DHDP monolayer without the additional release of Nd ions from DTPA by X-ray exposure.

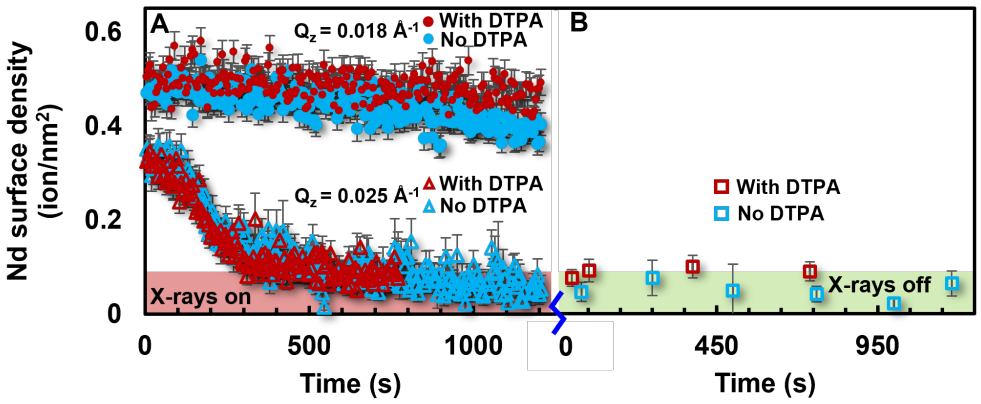

Figure 3. Irreversibility of Nd surface density at pH 2.0. A surface monolayer of DHDP was held at a surface pressure of 10 mN/m on the surface of water at pH 2.0 containing 10 μM $NdCl_3$ in the presence and absence of 30 μM DTPA. (A) X-rays-on condition: with (red) and without (blue) DTPA measured at Q_z = 0.018 Å^{-1} (top, dots) and Q_z = 0.025 Å^{-1} (bottom, triangles) (B) X-rays-off condition: measured at Q_z = 0.025 Å^{-1} with (red squares) and without (blue squares) DTPA. The data measured at Q_z = 0.018 Å^{-1} and at Q_z = 0.025 Å^{-1}, both with and without DTPA, were measured from different samples.

Figure 3B shows that the Nd surface density does not recover when X-rays are turned off and an adsorption cycle cannot be established. Figure 3A also shows that the Nd surface density measured at Q_z = 0.018 Å^{-1} is nearly constant with time when X-rays are confined to the surface. As before, the observation of a temporal variation in the Nd surface density when X-rays penetrate the

bulk, but not when X-rays are confined to the surface, indicates that aqueous radiolysis products are responsible for releasing Nd ions from the DHDP monolayer. However, the effect is irreversible suggesting that the X-ray exposure at this low pH is damaging the DHDP monolayer. Shifting the X-ray beam to a different position on the sample allows the Q_z = 0.025 Å^{-1} data shown in Fig. 3 to be reproduced (not shown), confirming that the change in Nd surface density observed at Q_z = 0.025 Å^{-1} is not due to changes in the entire surface, but is a local effect in the region of X-ray exposure. Similar observations for pH 2.25 and pH 2.5 samples are shown in Figs. S5 and S6.

Considerations on the X-ray exposure mechanism Although it is outside the scope of this paper to identify the full molecular scale mechanism that leads to the release of Nd ions from either DTPA or DHDP under X-ray exposure, several possibilities were explored. One possibility is that X-ray exposure reduces Nd^{3+} to Nd^{2+}, thereby weakening its binding. The oxidation state of 3+ for lanthanides, including Nd, is known to be stable under the solution conditions of these experiments,[31] however, it has been demonstrated that exposure to an ultra-high pressure mercury lamp can reduce the oxidation state to 2+.[32] The authors were successful in synthesizing insoluble Nd(II), Sm(II), and Eu(II) sulfates but were unable to produce Gd(II), citing its lower reduction potential. Nevertheless, if reduction to 2+ was the root cause of these X-ray induced results, the same transition is not expected to occur readily for Gd(III) due to its very stable half-filled 4*f*-shell.[33] Therefore, samples containing $GdCl_3$ substituted for $NdCl_3$ were used to test the role of lanthanide reduction in the observed X-ray effects. Measurements on pH 4.5 samples containing Gd^{3+} demonstrated a similar cyclical process as those with Nd^{3+} (Fig. S4), indicating that reduction of the lanthanide ion is not required for the X-ray exposure-induced adsorption cycle demonstrated by the data in Fig. 1.

Protonation of the amine group is unlikely at the pH values of the samples since the values of pKa for the three N groups of DTPA are 6, 7, and 8.[34] However, it has been shown that radiolysis products can cleave N-C and other bonds in ethylamine, triethylamine, and a diamide phenanthroline extractant.[25,35,36] It has also been reported that hydrated electrons and OH radicals induce the release of lanthanide and other ions from EDTA (ethylene diamine tetraacetic acid), a complexant similar in structure to DTPA.[37,38] A comparable attack of DTPA by aqueous radiolysis products would result in a loss of the coordination ability of the complexant.

The role of the N-C bond in the observed cycling was tested by substituting sodium citrate for DTPA. This substitution eliminates the nitrogen atoms from the chelate backbone and reduces the number of carboxyl groups from five to three. Both changes reduce the interaction of citrate with Nd.[39] To compensate for this reduced interaction and create a citrate sample whose behavior can be

compared with DPTA samples, the composition of citrate was chosen to be 10 mM at pH 6. Figure 4C shows that this composition yields a low surface density of Nd ions (0.02 ions nm^{-2}) when XFNTR is measured at Q_z = 0.018 $Å^{-1}$, for which X-rays illuminate only the surface. This demonstrates that Nd ions are nearly fully chelated by the citrate in bulk water under these conditions, like the nearly full chelation of Nd ions by DTPA demonstrated by XFNTR measured at Q_z = 0.018 $Å^{-1}$ in Fig. 4A which revealed a similar low surface density of 0.02 ions nm^{-2}. As shown in Fig. S7, reducing the pH of the citrate samples to pH 5 increases the Nd surface density to 0.1 ions nm^{-2}; therefore, pH 6 at 10 mM provides the condition at which citrate starts to nearly fully chelate Nd ions. Although it is likely that the composition of the DTPA samples (30 μM DTPA and pH 3.0 or 4.5) provides a slightly stronger chelation of Nd (compare Figures S1 and S8), the conditions chosen for citrate chelation should be at least equivalently susceptible, if not more so, to the release of Nd when X-rays expose the bulk water. Nevertheless, XFNTR measurements at Q_z = 0.025 $Å^{-1}$, for which X-rays illuminate both the surface and the bulk water, did not reveal an increase in surface density of Nd (Fig. 4C) in the presence of citrate, as observed for DTPA samples (shown in Fig. 4B and Fig. 1). These results suggest that the N-C bond in the backbone of DTPA is relevant for the mechanism of X-ray exposure-induced release of Nd ions.

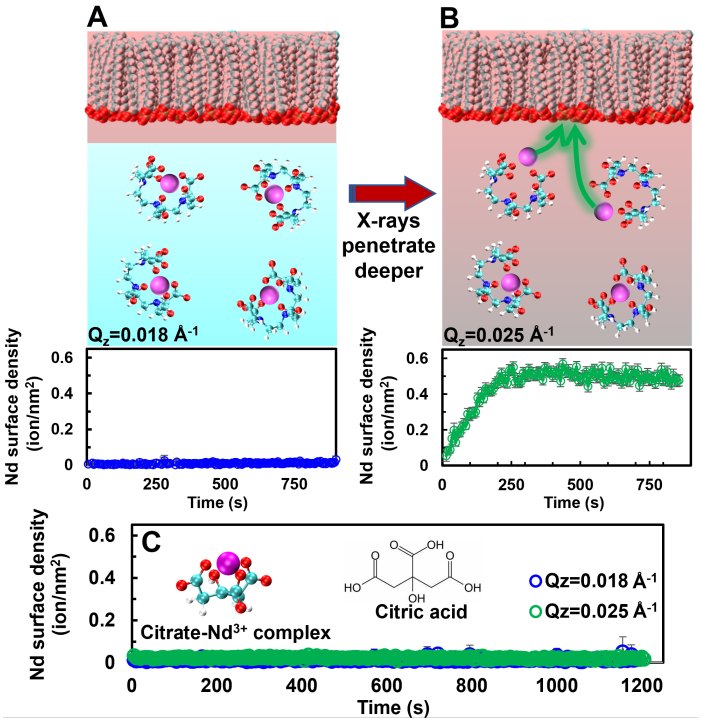

Figure 4. A comparison of citrate and DTPA chelation of Nd ions. Aqueous solutions measured in (A) and (B) contain 10 μM $NdCl_3$ and 30 μM DTPA at pH 4.5 with a DHDP monolayer spread at the surface and held at 10 mN/m. (A) Nd surface density under X-ray illumination at Q_z = 0.018 $Å^{-1}$, which

confines X-rays to an evanescent wave with a 10 nm penetration depth. (B) Nd surface density under X-ray illumination at Q_z = 0.025 Å^{-1}, for which X-rays transmit several micrometers into the bulk water. (C) Nd surface density of an aqueous solution containing 10 μM $NdCl_3$ and 10 mM trisodium citrate ($Na_3C_6H_5O_7$) at pH 6.0 with a DHDP monolayer spread at the surface and held at 10 mN/m. Measurements at Q_z = 0.018 Å^{-1} (blue) and Q_z = 0.025 Å^{-1} (green) overlap each other.

Conclusions

Reversible cycling of Nd ion adsorption to the surface of an aqueous solution was implemented by using X-ray exposure to alter the equilibrium between Nd bound to DTPA dissolved in bulk water and Nd bound to a monolayer of DHDP on the surface of the aqueous solution. Similar results were obtained for Gd ions and shown in the SI. A simple model described the measured temporal variation of ion surface density for X-rays-on and X-rays-off conditions. The derived kinetic rates correspond to time scales on the order of hundreds of seconds. We suggest that these long time processes are most likely dominated by diffusion effects of either ions, radiolysis products, or DTPA, because other processes should be much faster. X-ray exposure effects on the DHDP monolayer at pH 3.0 were due indirectly to radiolysis of bulk water, but at pH 4.5 an X-ray exposure process independent of radiolysis effects, possibly due to ozone production, was present. X-ray exposure effects on DTPA were due either indirectly to radiolysis of bulk water or to direct exposure of DTPA. Substitution of Gd ions for Nd ions suggested that reduction of rare earth ions by X-rays is not relevant to the observed cycling. Results obtained by substitution of trisodium citrate for DTPA suggested that the amines in DTPA are involved in the observed effects.

Reversible cycling was observed at pH 3 and 4.5. At lower pH, such as pH 2, the DTPA does not chelate a sufficiently large fraction of ions to deplete the DHDP monolayer of ions. Therefore, at lower pH, the bound fraction of ions to DHDP equilibrates essentially independently of the presence of DTPA in bulk solution.

Samples were exposed to X-rays in reflection geometry, which led to exposure of either the surface region alone or the surface plus bulk solution. The reflection geometry allowed for simultaneous exposure of the sample and measurement of the surface adsorption. Although reversible cycling of ion surface adsorption was observed only when the surface and bulk solutions were both exposed, because of the employed reflection geometry, the observed processes indicate that exposure of the bulk solution alone is likely to create reversible cycling of ion adsorption. In that case, cycling would require only x-ray exposure of the DTPA in the bulk solution. X-ray exposure would release Nd from DTPA which then binds to DHDP at the surface. When X-rays are turned off

the Nd would return to the DTPA because of the favored equilibrium binding between the two. X-ray exposure of the DHDP monolayer changed the shape of the measured curves but does not seem necessary for cycling ion adsorption. Although this has not yet been tested, it appears that exposing the bulk alone should cycle ions between bulk liquid and its surface, which could be relevant for applications.

The X-ray exposure process that produced reversible cycling of ion adsorption to a water-vapor interface could be used to supply ions in controlled doses to either a liquid-vapor or a liquid-liquid interface. Whether or not cycling will occur at a liquid-liquid interface would depend upon the behavior of the surfactant (or extractant) monolayer at the interface. If binding of ions to the surfactants (or extractants) leads them to extract ions into the second phase, then reversible cycling will not occur. However, if a surfactant monolayer remains at the interface upon ion binding, then reversible cycling can be expected at the liquid-liquid interface as well. In both cases, the observed effect of X-ray exposure can be used to controllably dose the interface with ions which could then subsequently trigger a range of interfacial effects, including metal ion extraction, catalysis, changes of interfacial phase or other properties.

Materials and Methods

Materials Ultrapure water from a Millipore system with resistivity of 18.2 MΩ·cm was used for all aqueous solutions. $NdCl_3 \cdot 6H_2O$ (99.9%), $GdCl_3 \cdot 6H_2O$ (99.995%), and chloroform (99.9%) were purchased from Sigma Aldrich. Dihexadecyl phosphoric acid (DHDP, >98%) was purchased from Avanti Polar Lipids Inc. Sodium hydroxide (NaOH, 98%) was purchased from Alfa-Aesar. Hydrochloric acid (HCl, 36.5 to 38.0%) and trisodium citrate dihydrate (99%) were purchased from Fisher Scientific. Chemicals were used as received without further purification.

Solution preparation Stock solutions of $NdCl_3$ (50 mM), $GdCl_3$ (50 mM), DTPA (100 mM) and trisodium citrate (100 mM) were prepared by dissolving them in ultrapure water. Further dilution produced the sample solutions. Aqueous pH of sample solutions was adjusted with diluted HCl or NaOH aqueous solutions. Chloroform solutions of DHDP (0.25 mM) were used to spread Langmuir monolayers.

X-ray flux conditions Aluminum absorber foils of 50 μm thickness were placed in the path of incoming X-rays prior to reflection from the interface to adjust the X-ray intensity as described in the SI. Ten foils were used in previous work, which did not show evidence of X-ray exposure effects.[20] Six

foils were used in the current work to yield a total X-ray flux on the sample of 3×10^{10} photons/s which created the observed effects.

XFNTR measurements A DHDP monolayer was formed in a Langmuir trough by spreading a DHDP-chloroform solution on the surface of aqueous solutions containing $NdCl_3$ (or $GdCl_3$) and DTPA, then compressed by a barrier to maintain a constant surface pressure of 10 mN/m. The trough vapor was purged of oxygen for roughly a half hour prior to measurements by flowing helium that had passed through an aqueous bubbler into the trough. Samples were exposed by reflecting 10 keV X-rays at small incident angles to achieve wave vector transfers of either Q_z = 0.018 Å^{-1} or Q_z = 0.025 Å^{-1}, where $Q_z = (4\pi/\lambda) \sin\theta$ for angle of incidence θ and X-ray wavelength λ . The X-ray fluorescence spectrum was recorded by a Vortex60-EX silicon drift energy dispersive detector placed perpendicularly above the surface. The X-ray fluorescence spectrum was normalized to the incident X-ray beam intensity and corrected for detector dead time. After normalization, the Lα1 X-ray fluorescence peak (Nd: 5255 eV; Gd: 6053 eV) was fit to a Gaussian function and a linear background to calculate the peak area, which provides the fluorescence signal.

Conventional XFNTR consists of X-ray fluorescence spectra measured for a range of wave vector transfer Q_z from below to above the critical Q_c for total reflection (Fig. S2D). [27] The XFNTR scan is then fit as previously described (Fig. S2D).[27,40] However, this method was unsuitable for the current work because each XFNTR scan requires at least several minutes to measure. Therefore, a single fluorescence spectrum was recorded at either Q_z = 0.018 Å^{-1} or Q_z = 0.025 Å^{-1} and the surface density analyzed from that spectrum, as described in Section S1 of the SI.

Acknowledgements

This research was performed using funding received from the U.S. Department of Energy, Office of Science, Office of Basic Energy Sciences Separations Program under Award Number DE-SC0018200 to MLS and from the National Science Foundation CHE-1834750 to NSF's ChemMatCARS. This material is also based upon work supported by the NNSA Minority Serving Institutions program under Award Number DE-NE0004008 to MLS, AG, and MAB. Use of the Advanced Photon Source, an Office of Science User Facilities operated for the U.S. Department of Energy (DOE) Office of Science by Argonne National Laboratory, was supported by the U.S. DOE under Contract No. DE-AC02-06CH11357.

Author Contributions

P.S., W.B., and M.L.S. initiated the project. P.S., W.B., M.L.S., M.A.B., A.V.G., M.K.B. and B.L. contributed to project design. M.A.B. and A.V.G. devised radiolysis tests and explanations. E.A.B. and B.S. assisted P.S. in X-ray measurements. The manuscript was prepared by M.L.S. and P.S. All authors discussed results and commented on the manuscript.

References

1 Lin, L. *et al.* Ion Pairing Mediates Molecular Organization Across Liquid/Liquid Interfaces. *ACS Applied Materials & Interfaces* **13**, 33734-33743 (2021). https://doi.org/10.1021/acsami.1c09763

2 Yin, X. *et al.* Ionic Layer Epitaxy of Nanometer-Thick Palladium Nanosheets with Enhanced Electrocatalytic Properties. *Chem. Mater.* **30**, 3308-3314 (2018). https://doi.org/10.1021/acs.chemmater.8b00575

3 Lund, M., Jungwirth, P. & Woodward, C. E. Ion Specific Protein Assembly and Hydrophobic Surface Forces. *Physical Review Letters* **100** (2008). https://doi.org/10.1103/PhysRevLett.100.258105

4 Chai, Y., Lukito, A., Jiang, Y., Ashby, P. D. & Russell, T. P. Fine-Tuning Nanoparticle Packing at Water–Oil Interfaces Using Ionic Strength. *Nano Letters* **17**, 6453-6457 (2017). https://doi.org/10.1021/acs.nanolett.7b03462

5 Scheu, R. *et al.* Specific Ion Effects in Amphiphile Hydration and Interface Stabilization. *J. Am. Chem. Soc.* **136**, 2040-2047 (2014). https://doi.org/10.1021/ja4120117

6 Wang, Z. *et al.* Ion sieving in graphene oxide membrane enables efficient actinides/lanthanides separation. *Nat. Commun.* **14** (2023). https://doi.org/10.1038/s41467-023-35942-1

7 Xia, X. *et al.* Unexpectedly efficient ion desorption of graphene-based materials. *Nat. Commun.* **13** (2022). https://doi.org/10.1038/s41467-022-35077-9

8 Amesh, P., Venkatesan, K. A., Suneesh, A. S. & Maheswari, U. Tuning the ion exchange behavior of cesium and strontium on sodium iron titanate. *Sep Purif Technol* **267** (2021). https://doi.org/10.1016/j.seppur.2021.118678

9 Zheng, S. P., Huang, L. B., Sun, Z. & Barboiu, M. Self-Assembled Artificial Ion-Channels toward Natural Selection of Functions. *Angew.Chem., Int. Ed.* **60**, 566-597 (2020). https://doi.org/10.1002/anie.201915287

10 Lu, J. *et al.* Efficient metal ion sieving in rectifying subnanochannels enabled by metal–organic frameworks. *Nat. Mat.* **19**, 767-774 (2020). https://doi.org/10.1038/s41563-020-0634-7

11 Jian, M. P. *et al.* Ultrathin water-stable metal-organic framework membranes for ion separation. *Sci Adv* **6** (2020). https://doi.org/10.1126/sciadv.aay3998

12 Gründer, Y., Ho, H. L. T., Mosselmans, J. F. W., Schroeder, S. L. M. & Dryfe, R. A. W. Inhibited and enhanced nucleation of gold nanoparticles at the water|1,2-dichloroethane interface. *Phys. Chem. Chem. Phys.* **13**, 15681-15689 (2011). https://doi.org/10.1039/C1CP21536A

13 Bera, M. K. *et al.* Interfacial transport and voltage-tunable arrays of charged nanoparticles. *Nano Letters* **14**, 6816-6822 (2014).

14 Zheng, B. Z. *et al.* Rare-Earth Doping in Nanostructured Inorganic Materials. *Chem Rev* **122**, 5519-5603 (2022). https://doi.org/10.1021/acs.chemrev.1c00644

15 He, Y., Zhou, W. & Xu, J. Rare Earth-Based Nanomaterials for Supercapacitors: Preparation, Structure Engineering and Application. *ChemSusChem* **15** (2022). https://doi.org/10.1002/cssc.202200469

16 Peng, F. *et al.* Hydrogen Clathrate Structures in Rare Earth Hydrides at High Pressures: Possible Route to Room-Temperature Superconductivity. *Physical Review Letters* **119** (2017). https://doi.org/10.1103/PhysRevLett.119.107001

17 Hossain, M. K. *et al.* Current Applications and Future Potential of Rare Earth Oxides in Sustainable Nuclear, Radiation, and Energy Devices: A Review. *ACS Applied Electronic Materials* **4**, 3327-3353 (2022). https://doi.org/10.1021/acsaelm.2c00069

18 Tasker, P. A., Plieger, P. G. & West, L. C. in *Comprehensive Coordination Chemistry II: From Biology to Nanotechnology* Vol. 9 (eds J. A. McCleverty & T.J. Meyer) 759-808 (Elsevier, 2004).

19 Huang, X. *et al.* Selective recovery of rare earth elements from ion-adsorption rare earth element ores by stepwise extraction with HEH(EHP) and HDEHP. *Green Chemistry* **19**, 1345-1352 (2017). https://doi.org/10.1039/c6gc03388a
20 Sun, P. *et al.* Antagonistic Role of Aqueous Complexation in the Solvent Extraction and Separation of Rare Earth Ions. *ACS Central Science* **7**, 1908-1918 (2021). https://doi.org/10.1021/acscentsci.1c00960
21 Nilsson, M. & Nash, K. L. A Review of the Development and Operational Characteristics of the TALSPEAK Process. *Solvent Extraction and Ion Exchange* **25**, 665–701 (2007). https://doi.org/10.1080/07366290701634636
22 Gelis, A. V. *et al.* Closing the Nuclear Fuel Cycle with a Simplified Minor Actinide Lanthanide Separation Process (ALSEP) and Additive Manufacturing. *Sci. Rep.* **9**, 1-11 (2019). https://doi.org/doi:10.1038/s41598-019-48619-x
23 Rydberg, J., Cox, M., Musikas, C. & Choppin, G. R. *Solvent Extraction Principles and Practice*. (Marcel Dekker, 2004).
24 Higgins, R. F., Ruoff, K. P., Kumar, A. & Schelter, E. J. Coordination Chemistry-Driven Approaches to Rare Earth Element Separations. *Accounts of Chemical Research* **55**, 2616-2627 (2022). https://doi.org/10.1021/acs.accounts.2c00312
25 Spinks, J. W. T. & Woods, R. J. *An Introduction to Radiation Chemistry*. Third Edition edn, (John Wiley & Sons, 1990).
26 Bobrowski, K., Skotnicki, K. & Szreder, T. Application of Radiation Chemistry to Some Selected Technological Issues Related to the Development of Nuclear Energy. *Topics in Current Chemistry* **374**, 60 (2016). https://doi.org/10.1007/s41061-016-0058-7
27 Bu, W. & Vaknin, D. X-ray fluorescence spectroscopy from ions at charged vapor/water interfaces. *J Appl Phys* **105**, 084911-084911 - 084911-084916 (2009). https://doi.org/Doi 10.1063/1.3117487
28 Ferradini, C. & Jay-Gerin, J.-P. The effect of pH on water radiolysis: A still open question — A minireview. *Research on Chemical Intermediates* **26**, 549-565 (2000). https://doi.org/10.1163/156856700x00525
29 Wang, W. J., Park, R. Y., Meyer, D. H., Travesset, A. & Vaknin, D. Ionic Specificity in pH Regulated Charged Interfaces: Fe^{3+} versus La^{3+}. *Langmuir* **27**, 11917-11924 (2011). https://doi.org/Doi 10.1021/La201880g
30 Kubota, F., Goto, M. & Nakashio, F. Extraction of rare earth metals with 2-ethylhexylphosphonic acid mono-2-ethylhexyl ester in the presence of diethyenetriaminepentaacetic acid in aqueous phase. *Solv. Extract. Ion Exch.* **11**, 437-453 (1993).
31 Takeno, N. Atlas of Eh-pH diagrams - Intercomparison of thermodynamic databases, Geological Survey of Japan Open File Report No.419. (National Institute of Advanced Industrial Science and Technology, Research Center for Deep Geological Environments, 2005).
32 Tsushima, S., Nagasaki, S. & Suzuki, A. Separation and Coprecipitation of Lanthanides and Americium by Photolysis. *Nuclear Technology* **118**, 42-48 (1997). https://doi.org/10.13182/nt97-a35355
33 Bunzli, J.-C. G. & Eliseeva, S. V. in *Lanthanide Luminescence: Photophysical, Analytical and Biological Aspects, Springer Series on Fluorescence* Vol. 7 (eds P. Hanninen & H. Ha¨ma) 1–46 (Springer-Verlag 2010).
34 Brown, M. A., Paulenova, A. & Gelis, A. V. Aqueous Complexation of Thorium(IV), Uranium(IV), Neptunium(IV), Plutonium(III/IV), and Cerium(III/IV) with DTPA. *Inorganic Chemistry* **51**, 7741-7748 (2012). https://doi.org/10.1021/ic300757k
35 Bibler, N. E. Gamma and alpha radiolysis of aqueous solutions of diethylenetriaminepentaacetic acid. *Journal of Inorganic and Nuclear Chemistry* **34**, 1417-1425 (1972). https://doi.org/https://doi.org/10.1016/0022-1902(72)80342-7

36 Chen, Y. *et al.* Radiolysis of diamide phenanthroline extractant: exploring the mechanism of HNO3 enhancing the extraction and An/Ln separation performance after irradiation. *Sep Purif Technol* **318**, 123994 (2023). https://doi.org/https://doi.org/10.1016/j.seppur.2023.123994
37 Anbar, M. & Meyerstein, D. Effect of ligands on reactivity of metal cations towards the hydrated electron, Part 1. The effect of ethylenediaminetetraacetic acid. *Transactions of the Faraday Society* **65**, 1812-1817 (1969).
38 Vel Leitner, N. K., Guilbault, I. & Legube, B. Reactivity of OH and e−aq from electron beam irradiation of aqueous solutions of EDTA and aminopolycarboxylic acids. *Radiation Physics and Chemistry* **67**, 41-49 (2003). https://doi.org/https://doi.org/10.1016/S0969-806X(02)00477-2
39 Brown, M. A., Kropf, A. J., Paulenova, A. & Gelis, A. V. Aqueous complexation of citrate with neodymium(iii) and americium(iii): a study by potentiometry, absorption spectrophotometry, microcalorimetry, and XAFS. *Dalton Transactions* **43**, 6446-6454 (2014). https://doi.org/10.1039/C4DT00343H
40 Bera, M. K. & Bu, W. XModFit: X-ray Modeling and Fitting. *Zenodo*, doi: https://doi.org/10.5281/zenodo.7047225 (2022). https://doi.org/10.5281/zenodo.7047225